ARTICLES
https://doi.org/10.1038/s41563-019-0387-3
nature materials

Diffraction imaging of nanocrystalline structures in organic semiconductor molecular thin films

Ouliana Panova[1,2,3,8], Colin Ophus[3,8], Christopher J. Takacs[4], Karen C. Bustillo[3], Luke Balhorn[5], Alberto Salleo[5], Nitash Balsara[2,6,7] and Andrew M. Minor[1,2,3*]

The properties of organic solids depend on their structure and morphology, yet direct imaging using conventional electron microscopy methods is hampered by the complex internal structure of these materials and their sensitivity to electron beams. Here, we manage to observe the nanocrystalline structure of two organic molecular thin-film systems using transmission electron microscopy by employing a scanning nanodiffraction method that allows for full access to reciprocal space over the size of a spatially localized probe (~2 nm). The morphologies revealed by this technique vary from grains with pronounced segmentation of the structure—characterized by sharp grain boundaries and overlapping domains—to liquid-crystal structures with crystalline orientations varying smoothly over all possible rotations that contain disclinations representing singularities in the director field. The results show how structure–property relationships can be visualized in organic systems using techniques previously only available for hard materials such as metals and ceramics.

The structure and morphology of any functional material can be directly correlated with its properties, including organic solids such as polymers and metal–organic frameworks[1–3]. However, direct imaging using conventional electron microscopy methods to study structural ordering at the level of individual defects and nanoscale domains is not routine for organic solids or other soft materials in the same manner as it is for inorganic or hard materials such as metals and ceramics. This difficulty is typically due to the complex (and often hierarchical) internal structure in organic solids and the inherent sensitivity to electron-beam-induced damage in organic materials. Thus, new and more robust methods for systematically investigating structure are necessary. Towards this end, we demonstrate the 'four-dimensional scanning transmission electron microscopy' (4D-STEM) technique[4] for the controlled, systematic and straight-forward investigation of nanoscale order in hierarchical, organized organic matter systems. As their electronic properties depend highly on their crystallographic geometry, organic semiconductors exemplify the need for improved understanding of the link between structural and functional properties in solid thin films across a multitude of length scales ideally suited for study by electron microscopy methods.

The low cost, low density, flexibility and manufacturability of polymers and organic molecular solids make them attractive materials for applications in photovoltaics[5–7], integrated circuits[8], light-emitting devices[9], bioelectronics and thermoelectrics, as alternatives to conventional metals and semiconductors. In well-performing organic semiconductors, both the molecular structure and processing must be extensively optimized for a particular application. Intramolecular electronic and excitonic transport is typically directed along the conjugated backbone of a molecular or polymeric system, while intermolecular interactions allow charges and excitons to couple across molecules and travel through larger scales[10–13]. It follows that the geometry and configuration of the molecules relative to one another dictate excitation transfer pathways. Understanding how low-dimensional and highly anisotropic semiconductors can form well-connected and robust morphologies remains a great challenge in the manipulation and creation of new topologies for the realization of increasingly efficient charge and energy transport in organic materials.

In this study, we characterized the nanostructure and defects of two organic semiconductor thin-film systems. The first is a small molecule, 7,7′-(4,4-bis(2-ethylhexyl)-4*H*-silolo[3,2-b:4,5-b′]dithiophene-2,6-diyl)bis(6-fluoro-4-(5′-hexyl[2,2′-bithiophen]-5-yl)benzo[c][1,2,5]-thiadiazole)[14], classically abbreviated as p-DTS(FBTTh$_2$)$_2$ in the literature, and in this Article denoted as T1, under two different processing conditions using 4D-STEM. The second system is a polymer thin film, poly[2,5-bis(3-tetradecylthiophen-2-yl)thieno[3,2-b]thiophene] (PBTTT)[15], both in the as-cast and annealed conditions. Our results demonstrate the ability to characterize the structure of organic materials with nanometre resolution using electron microscopy and show how the arrangement of nanoscale domains and their coupling from the nanoscale to mesoscale can be directly visualized for these types of materials system. This type of information is crucial for building structure–property relationships in this class of materials.

The small molecule under consideration (Fig. 1a) is a well-studied and well-performing electron donor and is responsible for exciton and hole transport when used in conjunction with an acceptor molecule, such as [6,6]-phenyl-C$_{70}$-butyric acid methyl ester[16] (PC$_{70}$BM) in bulk heterojunction materials with reported efficiencies up to 12%[12,17,18]. The material is known to undergo a lyotropic phase transition during the spincasting process that remains kinetically trapped in the thin film[19]. Polarization-dependent photoconductive atomic force microscopy (AFM) was able to map and estimate the local orientational order at a resolution of ~15 nm and complementary dark-field TEM experiments confirmed the

[1]Department of Materials Science and Engineering, University of California, Berkeley, CA, USA. [2]Materials Science Division, Lawrence Berkeley National Laboratory, Berkeley, CA, USA. [3]National Center for Electron Microscopy, Molecular Foundry, Lawrence Berkeley National Laboratory, Berkeley, CA, USA. [4]SLAC National Accelerator Laboratory, Menlo Park, CA, USA. [5]Department of Materials Science and Engineering, Stanford University, Palo Alto, CA, USA. [6]Department of Chemical and Biomolecular Engineering, University of California, Berkeley, CA, USA. [7]Joint Center for Energy Storage Research, Lawrence Berkeley National Laboratory, Berkeley, CA, USA. [8]These authors contributed equally: Ouliana Panova, Colin Ophus. *e-mail: aminor@lbl.gov

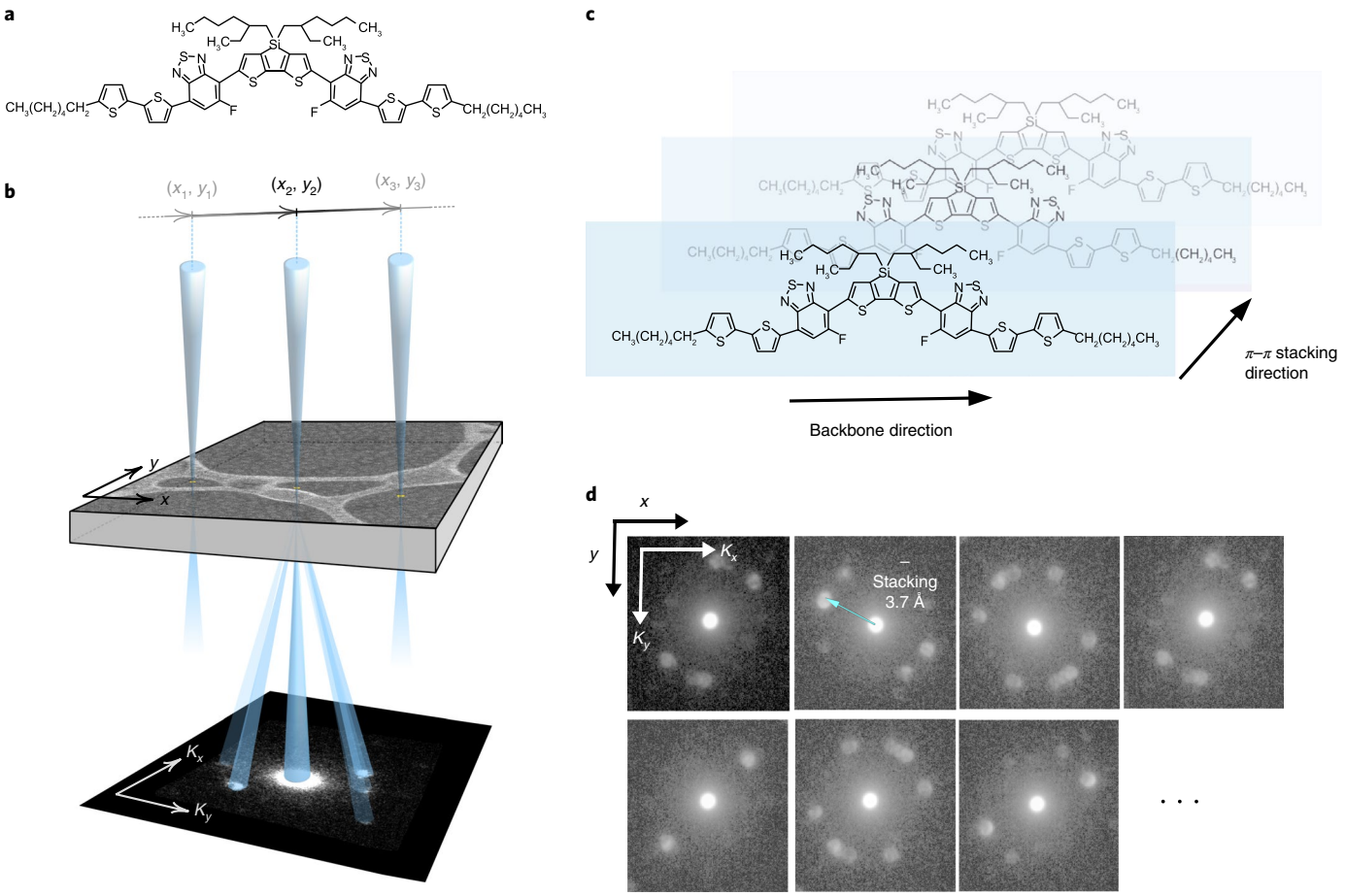

Fig. 1 | Schematic of the diffraction imaging technique. a,**b**, Molecular structure of the T1 molecule (**a**) and schematic of the 4D-STEM technique (**b**). As the convergent beam rasters over the area of interest, a full diffraction pattern is acquired for each real space probe location (*x*, *y*), with a step size large enough to prevent the beam from damaging the yet unsampled neighbouring positions. The molecules stack along their π–π bonds as illustrated in **c**. The data structure resulting from the technique is shown in **d**, with examples of diffraction patterns obtained from T1 + DIO (concentration 0.4%).

presence of a liquid-crystalline phase at an even coarser resolution[16]. However, due to the intrinsic and practical limitations of both methods, little is known about the structure on the nanometre scale, such as the morphology, size and mutual arrangement of the crystalline domains. When the samples are processed using a small concentration of the co-solvent 1,8-diiodooctane (DIO), the morphology and functional properties are significantly changed. In the poly(3-hexyl-thiophene-2,5-diyl) conducting polymer system it has been observed that the addition of DIO solvent affects a number of morphological and electronic characteristics of the polymer film[20]. Samples treated with certain concentrations of DIO have shown a decreased viscosity and surface roughness under AFM[21]. The addition of DIO ultimately appears to contribute to a more compact packing of the donor and acceptor phases and an overall more homogeneous film morphology[22]. When DIO was added to a blend of T1 and $PC_{70}BM$, a maximum photocurrent efficiency (PCE) was found for 0.4% DIO, and the addition of $PC_{70}BM$ in large quantities appears to disrupt the crystallinity of T1[23]. Most recently it has been reported that the addition of DIO to a similar donor small molecule converts the normally in-plane direction of the backbone to a 50:50 in-plane:out-of-plane orientation of the backbone[24]. However, the nature and spatial distribution of any morphological changes have yet to be explored at high resolution.

Two samples of the T1 molecule, one with DIO treatment (T1 + DIO) and one without, were imaged using the 4D-STEM technique, shown schematically in Fig. 1b. The fragile nature of the samples' crystallinity under the electron beam presents a significant challenge, as did the relatively weak diffraction from the ordered domains. To reduce beam damage, the samples were cooled with liquid nitrogen and the acquisition parameters were empirically tuned to obtain the best diffraction signal possible; a step size of 10 nm was found to be the limit below which the beam started damaging the crystallinity of sample regions not yet exposed to the electron beam, providing the spatial resolution limit for any image resulting from the data (sample preparation and image acquisition parameters are detailed in the Methods). A representative sampling of the diffraction patterns (DPs) obtained are shown in Fig. 1d. Most probe locations exhibited at least one diffraction spot pair corresponding to an in-plane ~3.7 Å π–π spacing of the T1 molecule, indicating a textured thin film.

Figure 2 shows how 4D-STEM can extract previously unseen structural information about the small-molecule thin film. The traditional high-angle annular dark field (HAADF) images acquired during a standard capture (square images, Fig. 2a,b) provide effectively no information about the film's structure. Likewise, virtual dark-field reconstructions measuring the brightness of an annular ring equivalent to the π–π spacing of the T1 molecule (rectangular images, Fig. 2a,b) do not provide any information that can be directly related to the properties of the material. In contrast, the 4D-STEM technique can reveal the underlying structure of the small-molecule films by assigning every pixel of a raster scan to a specific in-plane crystal orientation or distribution of crystal

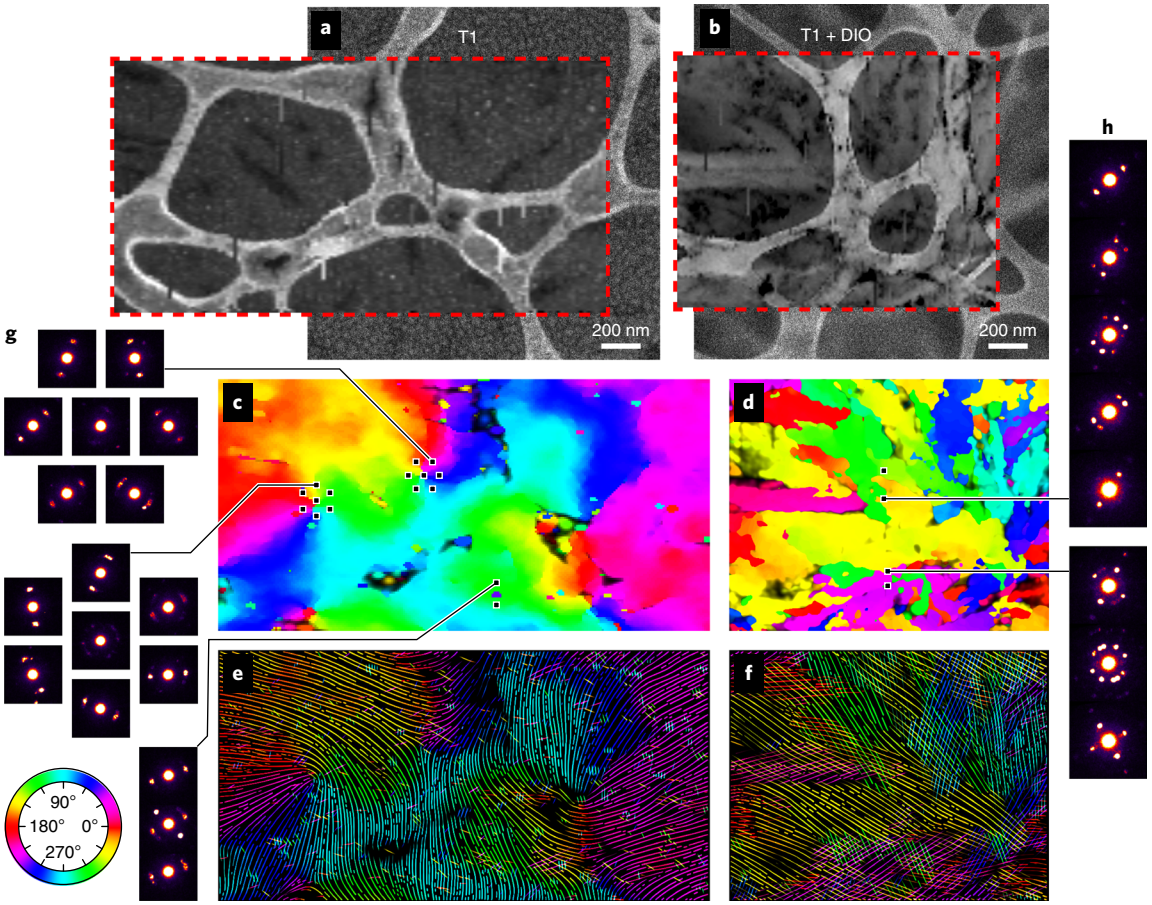

Fig. 2 | Comparison of grain morphology between DIO samples. a–h, The panels on the left (**a**,**c**,**e**,**g**) are from the sample dropcast without DIO and the panels on the right (**b**,**d**,**f**,**h**) are from the sample dropcast with DIO. **a**,**b**, The background HAADF images show few, if any, of the molecular film details; the web-like features are components of the supporting lacey carbon grid. Dashed lines represent the area over which the 4D-STEM scan was performed. Within the scan areas, a virtual dark field is overlaid onto the HAADF. **c**,**d**, The orientation maps show the direction of the brightest reflection found at that location. **e**,**f**, Flow line maps trace the molecular backbone structure, with the T1 sample demonstrating gradual lattice rotations while the T1 + DIO sample shows rigid crystalline domains with significant overlap. **g**, Example diffraction patterns from the T1 sample showing disclinations of opposite sign, and an example of a small overlapping fragment. **h**, Example diffraction patterns from the T1 + DIO showing multiple overlapping grain orientations.

orientations[25] (details of the data analysis are provided in the Methods). Mapping the angle of orientation of the brightest π–π diffraction spot pair for each probe location reveals the impact of DIO on the morphology of the polymer. The sample left to dry without DIO exhibits a structure akin to that of liquid crystals[26], with ordered domains smoothly twisting over the whole 180° range and over length scales of ~100 nm (Fig. 2c). Of note are the topological defects that can be visualized (indicated by a subset of diffraction patterns in Fig. 2g). These singularities represent defect structures called disclinations, which have been extensively modelled[27,28] and previously observed for this system[16]. Figure 2g shows examples of both $+\frac{1}{2}$ and $-\frac{1}{2}$ disclinations. Additionally, small overlapping fragments are visible over the entire field of view, with diameters ranging from 10 to 50 nm. The diffraction signals from these grains do not interrupt the larger smoothly twisting grains, indicating that they are located either above or below the primary features.

By contrast, the sample treated with DIO shows a sharply segmented grain structure, with clearly defined grain boundaries and identifiable domains of closely similar orientations that extend over hundreds of nanometres, as seen in Fig. 2d. Although there is still an ~5–10° internal fluctuation in orientation within the grains due to the flexible nature of the molecule, the crystalline domains are now very clearly defined. Low-angle grain boundaries and small angular fluctuations are known to maintain electronic coupling between neighbouring domains better than random orientations[29]. The DPs for this sample also exhibit several distinct lattice reflections at certain probe locations that persist over dozens of real space positions, providing demonstrative evidence that distinct crystalline domains overlap through the film thickness of this sample on the sample size of the probe. Although it is not possible to determine the order of the grains along the beam direction (through the thickness of the film), the line plots presented in Fig. 2e,f, visualized using flow line methods (often seen in fluid dynamics measurements)[30], allow us to visualize the molecular chains and understand the continuity of the structure, as each lattice reflection found at (x, y) is represented by a line coloured and oriented according to its lattice orientation angle θ. The lines in these drawings are oriented perpendicular to their reciprocal space reflections and presumably align with the molecular long axis in real space. Although the density of the lines is not indicative of the lattice spacing, their orientation and extent are a direct illustration of the local orientation of the lattice planes, also called the director field[31].

In the T1 + DIO sample, many overlapping domains are visible. Most domains tend to be elongated along a direction close to the molecular backbone axis. Most of the larger domains have a longer axial dimension on the order of micrometres, and a shorter axial dimension of 100–400 nm. Topological singularities were not observed in this sample, but small backbone rotations were observed inside some of the grains (usually <13°). The domains

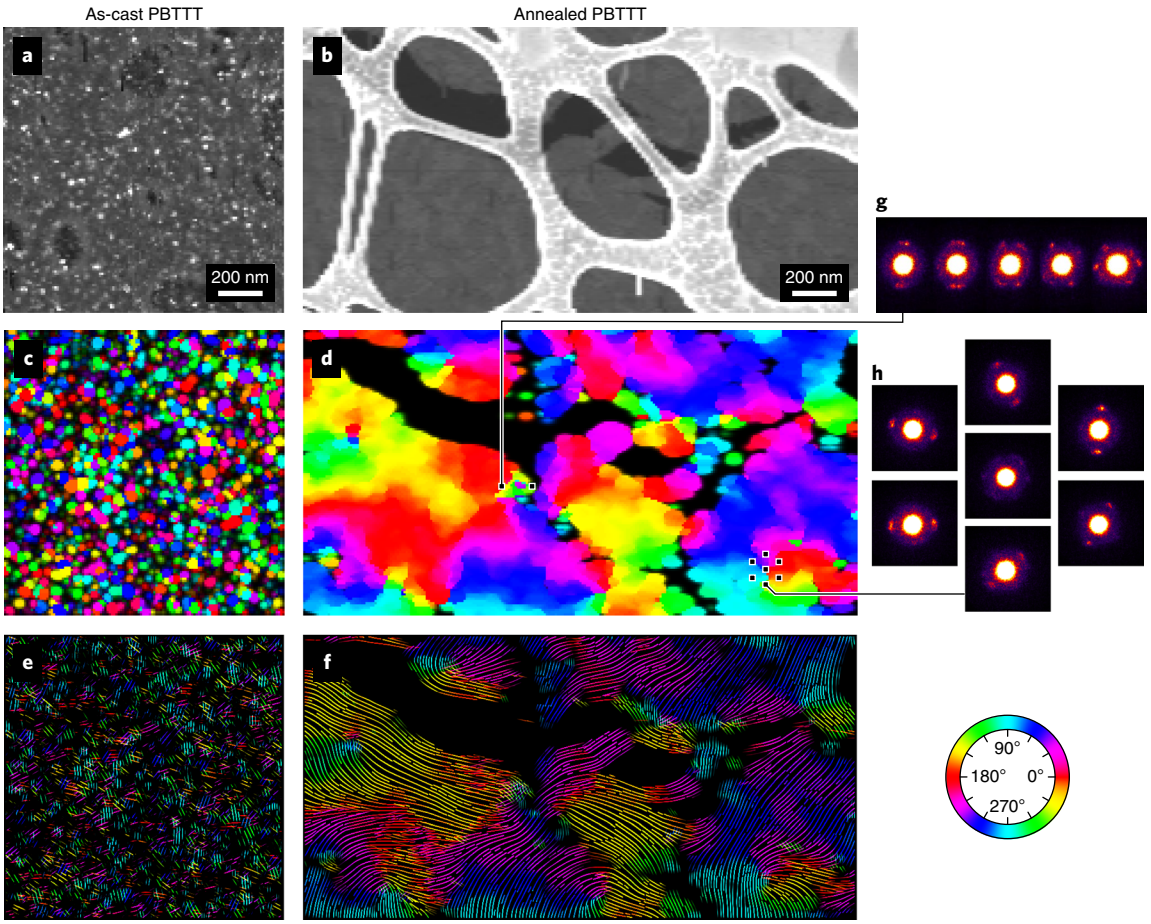

Fig. 3 | Comparison of grain morphology between PBTTT samples. a,**b**, Virtual dark-field reconstructions of as-cast and annealed PBTTT thin films, respectively. **c**–**f**, Orientation (**c**,**d**) and flow line (**e**,**f**) maps corresponding to **a**,**b**, respectively. **g**,**h**, Example diffraction patterns of annealed PBTTT showing overlapping grain orientations (**g**) and a disclination (**h**).

had a slight preferred orientation, but domains stacked along the beam direction did not appear to have any simple crystallographic orientation relationship.

A study of the microstructure of the PBTTT polymer[15] as a function of annealing conditions showcases the potential of the 4D-STEM technique in providing insights into the structure–property relationships relevant for organic field-effect transistors. The as-cast carrier mobility of PBTTT in field-effect transistors is on the order of 0.01–0.1 $cm^2 V^{-1} s^{-1}$. PBTTT exhibits a liquid-crystalline mesophase in a temperature range determined by the length of its alkyl side chains. We studied the material with 14-carbon-atom-long side chains, which exhibits the mesophase between 140 °C and 248 °C on heating in the bulk. After annealing the film into the mesophase, the mobility increases up to 1 $cm^2 V^{-1} s^{-1}$ and dramatic microstructural changes are observed by X-ray diffraction and AFM. In particular, annealing leads to an increase in the diffraction signal and the formation of large terraces, indicating an enhancement in order of the material. We fabricated films following the same protocol and thicknesses used to make thin-film transistors and then transferred them to a TEM grid for microstructural characterization. To compare the microstructures we studied two conditions: as-cast and annealed in the liquid-crystal phase at 180 °C.

The construction of flow line maps, as explained earlier, reveals dramatic differences in the microstructure at the mesoscale (Fig. 3), which are correlated with the charge transport properties of the films. In the as-cast film, no mesoscale order is observed. When annealed in the mesophase, the polymer shows enhanced mesoscale ordering with domains spanning hundreds of nanometres. Interestingly, the regions of order blend smoothly into each other by continuous backbone deformation similar to the T1 sample, clearly seen by comparing Figs. 2e and 3f. Orientational correlation is an important functional parameter in PBTTT. Indeed, using polarized soft X-ray scattering, it has been shown that the mobility in PBTTT thin films correlated with backbone orientational correlation[32]. Although polarized soft X-rays do not require crystalline material and are a powerful method for investigating orientational order, the dipole nature of the interaction precludes distinguishing between amorphous material and well-ordered layers overlapping at high angles. In comparison, a 4D-STEM data set provides additional information on the heterogeneity of the microstructure and can provide a great wealth of quantitative microstructural properties.

The morphological differences are further emphasized in the autocorrelation study shown in Fig. 4. By correlating the lattice orientations at each probe location to those of all other probe locations, a map of the probability of finding the same orientation at a distance Δr and a misorientation $\Delta\theta$ is computed according to the autocorrelation function:

$$C(\Delta r, \Delta\theta) = \frac{\langle I(r, \theta) I(r+\Delta r, \theta+\Delta\theta)\rangle_{r,\theta}}{\langle I(r,\theta)\rangle^2_{r,\theta}}$$

where $I(r,\theta)$ is the measured intensity of the orientation distribution of the lattice vectors, $\langle\ldots\rangle_{r,\theta}$ is an average over all equal radii

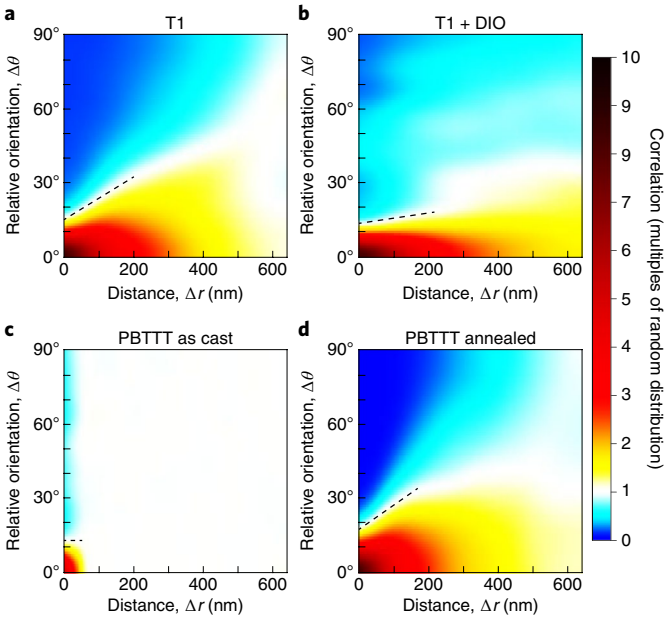

Fig. 4 | Autocorrelation of the primary lattice vectors over distance Δ*r* and relative orientation Δ*θ*, for the films characterized in Figs. 2 and 3. **a**–**d**, Autocorrelation for T1 (**a**), T1 + DIO (**b**), as-cast PBTTT (**c**) and annealed PBTTT (**d**) samples. Correlations are normalized to units of randomly oriented grains, and an overlaid dashed line shows the trend where the measured correlation is equivalent to a random distribution for small distances.

and orientations, and $\langle I(r,\theta)\rangle^2_{r,\theta}$ represents a normalization factor equivalent to a completely random distribution of lattice orientations in real space. The value of $C(\Delta r,\Delta\theta)$ therefore indicates the correlation between probe locations, with observation probability units relative to a random distribution of orientations. Thus, each vertical slice in Fig. 4 represents a histogram of orientation differences at a given separation distance. The red end of the spectrum ($C>1$) shows orientation differences that are more likely than average to occur. In contrast, the blue end of the spectrum shows angles that are less likely than average to occur—in the small fraction of cases when they do occur, it is probably across a grain boundary. Thus, the breakeven point between these two regions, shown as a dashed line in Fig. 4, approximates the maximum orientation differences that can be tolerated within a single grain. The slope of this line is then related to the degree of curvature present within grains.

The autocorrelation of the T1 sample in Fig. 4a shows a smooth transition in both Δr and $\Delta\theta$, with the spread of $\Delta\theta$ increasing almost linearly with increasing distance Δr. This feature corresponds to the slowly varying orientation of the lattice planes over large distances visible in Fig. 2e, and is shown in Fig. 4a by a dashed line drawn where the correlation is equal to a random distribution. By contrast, the T1 + DIO correlation plotted in Fig. 4b shows a sharp drop-off around $\Delta\theta = 15°$, indicating that misorientations within most grains do not exceed that value. The secondary transition point seen on the T1 + DIO map at $\sim\Delta\theta = 30°$ indicates that neighbouring and overlapping grains tend to have misorientations below 30–40° over all distances measured. This can also be seen by the dashed line in Fig. 4b, which shows only a small increase with distance, indicating that the grains do not contain the varying in-grain orientations measured in Fig. 4a. The in-grain lattice plane bending seen in the untreated sample's lattice is the result of a kinetically locked pseudo-phase, and is consistent with the observation that films without DIO dry much faster than ones with DIO[33,34].

Figure 4c shows the correlation map of the primary lattice for the as-cast PBTTT sample. Beyond distances of $\Delta r = 50$ nm, no correlation is visible, which indicates that this sample is composed of small, randomly oriented grains. In comparison, the lattice plane correlation of the annealed PBTTT sample shown in Fig. 4d shows very long-range correlations, very similar to those measured for the T1 sample in Fig. 4a. This is unsurprising, given the morphological similarities of the structures measured in Figs. 2e and 3f. Similarly, the dashed line shown in Fig. 4d indicates that the grains have a slowly varying lattice orientation $\Delta\theta$ that is approximately linear with distance Δr. The correlation measurements in Fig. 4 demonstrate that much of a polymer sample's orientation and morphology can be summarized by correlation measurements, which could facilitate their comparison to deposition and growth models.

The ability to simultaneously obtain information at the nanometre scale and at the mesoscale up to several micrometres is a very advantageous feature of 4D-STEM over other traditional electron microscopy techniques[35] as charge transport in polymers notoriously depends on processes occurring at many length scales[36]. For instance, backbone flow field maps can be used as the starting point for realistic charge transport simulations, revealing what defects in the films give rise to bottlenecks[37].

We have successfully resolved and mapped the local crystalline nanostructure of two semiconducting small-molecule and polymer thin-film systems using the 4D-STEM technique. Exposure of the T1 system to DIO during casting dramatically alters the nanostructure of the resulting material, moving from a smectic liquid-crystal-like, continuous, smoothly twisting film to a partially segmented, overlapping discrete grain structure. In the PBTTT system, annealing led to a similar effect. The nanocrystalline morphologies of both systems have been analysed through automated algorithms to gain insight into the differences between the two structures and to relate the structure to the kinetic and energetic pathways of formation. The flexible nature of the 4D-STEM technique, as well as its ability to be applied to any semicrystalline or ordered organic material[38], facilitate measurement and comparison of phase morphology in these organic materials at a spatial resolution not previously possible.

Online content

Any methods, additional references, Nature Research reporting summaries, source data, statements of code and data availability and associated accession codes are available at https://doi.org/10.1038/s41563-019-0387-3.

Received: 15 November 2018; Accepted: 23 April 2019;
Published online: 3 June 2019

References

1. Van Krevelen, D. W. & Te Nijenhuis, K. *Properties of Polymers: Their Correlation with Chemical Structure; Their Numerical Estimation and Prediction from Additive Group Contributions* (Elsevier, 2009).
2. Wilmer, C. E. et al. Large-scale screening of hypothetical metal–organic frameworks. *Nat. Chem.* **4**, 83–89 (2012).
3. Fratini, S., Ciuchi, S., Mayou, D., de Laissardière, G. T. & Troisi, A. A map of high-mobility molecular semiconductors. *Nat. Mater.* **16**, 998–1002 (2017).
4. Ophus, C. Four dimensional scanning transmission electron microscopy: from scanning nanodiffraction to ptychography and beyond. *Microsc. Microanal.* **25**, 563–582 (2019).
5. Kim, J. H. et al. Optimization and analysis of conjugated polymer side chains for high-performance organic photovoltaic cells. *Adv. Funct. Mater.* **26**, 1517–1525 (2016).
6. Li, G. et al. High-efficiency solution processable polymer photovoltaic cells by self-organization of polymer blends. *Nat. Mater.* **4**, 864–868 (2005).
7. Zhao, W. et al. Fullerene-free polymer solar cells with over 11% efficiency and excellent thermal stability. *Adv. Mater.* **28**, 4734–4739 (2016).
8. Smits, E. C. P. et al. Bottom-up organic integrated circuits. *Nature* **455**, 956–959 (2008).
9. Di, D. et al. Efficient triplet exciton fusion in molecularly doped polymer light-emitting diodes. *Adv. Mater.* **29**, 1605987 (2017).
10. Salaneck, W. R., Friend, R. H. & Brédas, J. L. Electronic structure of conjugated polymers: consequences of electron–lattice coupling. *Phys. Rep.* **319**, 231–251 (1999).

11. Collini, E. & Scholes, G. D. Coherent intrachain energy migration in a conjugated polymer at room temperature. *Science* **323**, 369–373 (2009).
12. Sirringhaus, H. et al. Two-dimensional charge transport in self-organized, high-mobility conjugated polymers. *Nature* **401**, 685–688 (1999).
13. Lemaur, V., Steel, M., Beljonne, D., Brédas, J.-L. & Cornil, J. Photoinduced charge generation and recombination dynamics in model donor/acceptor pairs for organic solar cell applications: a full quantum-chemical treatment. *J. Am. Chem. Soc.* **127**, 6077–6086 (2005).
14. Zhang, L. et al. Poly(3-butylthiophene) inducing crystallization of small molecule donor for enhanced photovoltaic performance. *J. Phys. Chem. C* **119**, 23310–23318 (2015).
15. McCulloch, I. et al. Liquid-crystalline semiconducting polymers with high charge-carrier mobility. *Nat. Mater.* **5**, 328–333 (2006).
16. Takacs, C. J. et al. Mapping orientational order in a bulk heterojunction solar cell with polarization-dependent photoconductive atomic force microscopy. *ACS Nano* **8**, 8141–8151 (2014).
17. Dennler, G., Scharber, M. C. & Brabec, C. J. Polymer-fullerene bulk-heterojunction solar cells. *Adv. Mater.* **21**, 1323–1338 (2009).
18. Zhao, W., Li, S., Zhang, S., Liu, X. & Hou, J. Ternary polymer solar cells based on two acceptors and one donor for achieving 12.2% efficiency. *Adv. Mater.* **29**, 1604059 (2017).
19. Maged, A. et al. Toward additive-free small-molecule organic solar cells: roles of the donor crystallization pathway and dynamics. *Adv. Mater.* **27**, 7285–7292 (2015).
20. Arca, F., Loch, M. & Lugli, P. Enhancing efficiency of organic bulkheterojunction solar cells by using 1,8-diiodooctane as processing additive. *IEEE J. Photovolt.* **4**, 1560–1565 (2014).
21. Reichenberger, M. et al. Watching paint dry: the impact of diiodooctane on the kinetics of aggregate formation in thin films of poly(3-hexylthiophene). *Macromolecules* **49**, 6420–6430 (2016).
22. Herath, N. et al. Unraveling the fundamental mechanisms of solvent-additive-induced optimization of power conversion efficiencies in organic photovoltaic devices. *ACS Appl. Mater. Interfaces* **8**, 20220–20229 (2016).
23. Van Der Poll, T. S., Love, J. A., Nguyen, T. Q. & Bazan, G. C. Non-basic high-performance molecules for solution-processed organic solar cells. *Adv. Mater.* **24**, 3646–3649 (2012).
24. Brown, S. J. et al. Enhancing organic semiconductor–surface plasmon polariton coupling with molecular orientation. *Nano Lett.* **17**, 6151–6156 (2017).
25. Panova, O. et al. Orientation mapping of semicrystalline polymers using scanning electron nanobeam diffraction. *Micron* **88**, 30–36 (2016).
26. Frank, F. C. I. Liquid crystals. On the theory of liquid crystals. *Discuss. Faraday Soc.* **25**, 19–28 (1958).
27. Meyer, R. B. On the existence of even indexed disclinations in nematic liquid crystals. *Philos. Mag.* **27**, 405–424 (1973).
28. Saupe, A. Disclinations and properties of the directorfield in nematic and cholesteric liquid crystals. *Mol. Cryst. Liq. Cryst.* **21**, 211–238 (2007).
29. Jimison, L. H., Toney, M. F., McCulloch, I., Heeney, M. & Salleo, A. Charge-transport anisotropy due to grain boundaries in directionally crystallized thin films of regioregular poly(3-hexylthiophene). *Adv. Mater.* **21**, 1568–1572 (2009).
30. Merzkirch, W. *Flow Visualization* (Elsevier, 2012).
31. Wood, B. A. & Thomas, E. L. Are domains in liquid crystalline polymers arrays of disclinations? *Nature* **324**, 655–657 (1986).
32. Collins, B. A. et al. Polarized X-ray scattering reveals non-crystalline orientational ordering in organic films. *Nat. Mater.* **11**, 536–543 (2012).
33. Qian, L. et al. Effect of crystallinity of fullerene derivatives on doping density in the organic bulk heterojunction layer in polymer solar cells. *Chin. Phys. Lett.* **32**, 056801 (2015).
34. Yang, X. et al. Crystalline organization of a methanofullerene as used for plastic solar-cell applications. *Adv. Mater.* **16**, 802–806 (2004).
35. Takacs, C. J. et al. Remarkable order of a high-performance polymer. *Nano Lett.* **13**, 2522–2527 (2013).
36. Rivnay, J., Mannsfeld, S. C. B., Miller, C. E., Salleo, A. & Toney, M. F. Quantitative determination of organic semiconductor microstructure from the molecular to device scale. *Chem. Rev.* **112**, 5488–5519 (2012).
37. Mollinger, S. A., Krajina, B. A., Noriega, R., Salleo, A. & Spakowitz, A. J. Percolation, tie-molecules, and the microstructural determinants of charge transport in semicrystalline conjugated polymers. *ACS Macro Lett.* **4**, 708–712 (2015).
38. Mohammadi, E. et al. Dynamic-template-directed multiscale assembly for large-area coating of highly-aligned conjugated polymer thin films. *Nat. Commun.* **8**, 16070 (2017).

Acknowledgements

Primary funding for the work was provided by the Electron Microscopy of Soft Matter Program from the Office of Science, Office of Basic Energy Sciences, Materials Sciences and Engineering Division of the US Department of Energy under contract no. DE-AC02-05CH11231. Work at the Molecular Foundry was supported by the Office of Science, Office of Basic Energy Sciences, of the US Department of Energy under contract no. DE-AC02-05CH11231. L.B. and A.S. acknowledge funding from the National Science Foundation DMR Award no. 1808401. The authors also thank H. Yan for providing materials and M. Toney for useful discussions.

Author contributions

A.M.M. and N.B. conceived of the project. C.J.T., L.B. and O.P. prepared the samples. O.P. and K.C.B. designed the experiment and acquired the data. C.O., O.P., K.C.B., C.J.T., L.B., A.S. and A.M.M, analysed the data and all authors contributed to writing the manuscript.

Competing interests

The authors declare no competing interests.

Additional information

Reprints and permissions information is available at www.nature.com/reprints.

Correspondence and requests for materials should be addressed to A.M.M.

Publisher's note: Springer Nature remains neutral with regard to jurisdictional claims in published maps and institutional affiliations.

Methods

Sample preparation and microscopy. T1 samples were dissolved in chlorobeneze (20 mg mL^{-1} at 60 °C). A 0.4% DIO solution was added to one of the samples before both were blade coated (35 mm s^{-1}) onto a PEDOT:PSS coated silicon substrate (held at 35 °C). The PEDOT:PSS layer was dissolved in DI water and the film was delaminated onto the air/water interface. A loop tool was used to transfer the films to the TEM grid and the residual water was allowed to evaporate. The PBTTT (M_n = 19 kDa, polydispersity index = 1.3) samples were prepared through spincasting. Silicon substrates with 200 nm thermal oxide were cleaned by sonicating in acetone, methanol and isopropanol for 15 min each. The substrates were then treated with an octyltrichlorosilane self-assembled monolayer after a 20 min ultraviolet–ozone exposure. Films of PBTTT were spincast from a 2 mg ml^{-1} solution in chlorobenzene. The solution was heated to 80 °C. The films were then spun at 800 r.p.m. for 1 min. Annealed films were heated for 2 h at 180 °C, then cooled on a steel heatsink. Spin-coating and annealing were performed in a nitrogen glovebox (O_2 of <1 ppm). Films were transferred onto ultrathin carbon/lacey carbon TEM grids via liftoff in dilute hydrofluoric acid and floating onto a deionized water/air interface.

The nanodiffraction data sets were collected using a Gatan Orius charge-coupled device on an FEI TitanX microscope at 300 kV operated in STEM mode with a small convergence semi-angle of α = 0.48 mrad and a camera length of 380 mm. The Gaussian-shaped probe size was measured to be 2.0 nm at full-width at half-maximum (FWHM). Because the undiffracted central spot was needed for realignment of the diffraction patterns, and to avoid masking any diffraction spots, no beam stop was used. The spots on the diffraction patterns are large in part due to the relatively convergent nature of the beam and average ~24 pixels in diameter on the detector. Having large but non-overlapping spots on the diffraction pattern presents an advantage when performing template matching, as the locations of the spots can be determined quite robustly.

The samples were cooled with liquid N_2 to mitigate beam damage to the long-range order during data collection. Because beam exposure of an area destroys its crystallinity, locations for data collection were determined semi-blindly. The sample was surveyed in STEM diffraction mode until a place with strong lattice reflection spots was found, at which point the beam was blanked. The goniometer was then moved by a few micrometres away from the damaged area, and the 4D-STEM acquisition launched immediately after un-blanking the beam. Diffraction patterns were obtained at an empirically determined minimum step size of 10 nm over an area of 128 × 128 pixels, with an acquisition time of 33 ms. These parameters were empirically determined to provide the best signal-to-noise ratio on the diffraction patterns. Longer exposure times led to destruction of sample crystallinity. Shorter step sizes led the beam to prematurely damage areas that had yet to be sampled. Even though the probe size at FWHM was smaller than the 10 nm step size, the damage incurred by the secondary electrons as they percolate laterally through the sample and cause damage ahead of the probe put a limit on how close the probe locations could be without seeing the diffraction spots disappear.

The dose or fluence (in e^- Å^{-2}) that the sample receives can be estimated using two approaches: (1) calculate the average dose over the entire scanned area or (2) calculate the dose as if all the beam current is spread over an area defined by the FWHM of the probe. Using the first method, a beam current of 5 pA with a step size of 10 nm and an exposure of 33 ms translates into an average dose of ~100 e$^-$ Å^{-2} for the nanobeam diffraction experiment in this work. A typical HAADF-STEM image of 50 pA, 12 µs dwell time and 2 Å pixel size corresponds to a dose of ~1,000 e^- Å^{-2}. As compared with one STEM image, the nanobeam diffraction exposes the sample to an order of magnitude less dose. Using the second method, a beam current of 5 pA covering the area of a circle of 2 nm (FWHM of probe) with an exposure of 33 ms translates into a dose of ~3,000 e^- Å^{-2} for the nanobeam experiment.

Data analysis. The 4D-STEM data were processed in Matlab to extract the diffraction spot positions at every pixel. The general peak finding method has been described in a previous publications[25,39]. Because the 4D-STEM experiment covered a relatively large field of view, a small linear shift of the diffraction pattern was observed as a function of the probe x and y positions. This shift was measured by fitting the position of the unscattered centre disk in all diffraction images, which was set to the origin position $(K_x,K_y) = 0$ for each diffraction image. The centre disk was averaged (after correcting for origin shifts) and used as a template $I_{\mathrm{ref}}(K_x,K_y)$ for hybrid correlation fitting of all scattered and unscattered Bragg disk positions in all images $I(K_x,K_y)$, using the expression

$$P(K_x, K_y) = \mathcal{F}^{-1}\left\{\frac{\mathcal{F}\{I(K_x, K_y)\} \cdot \mathcal{F}\{I_{\mathrm{ref}}(K_x, K_y)\}^*}{|\mathcal{F}\{I(K_x, K_y)\} \cdot \mathcal{F}\{I_{\mathrm{ref}}(K_x, K_y)\}^*|^{0.1}}\right\}$$

where local maxima of $P(K_x,K_y)$ represent locations on each diffraction image where the template and the image have a good match. The minimum angular spacing where unique disks with the same diffraction length vector could be identified is ~5°. The radial bin width for selecting the d spacing was ±8.5% for the T1 molecule and ±10% for the PBTTT.

Trace flow visualizations were made by propagating lines across the field of view. At each real space position r_1 a seed for every found orientation θ_1 is initiated and a line propagated (at a ±90° angle) to its adjoining pixel r_2, wherein it takes on the orientation θ_2 of the orientation closest to θ_1. The line is stopped if no close orientations are found, or if it overlaps with previously calculated flow lines (with a relative orientation $\Delta\theta < 5°$) within a minimum distance of a few pixels. This procedure generates a field of approximately equally spaced flow lines, for all orientations detected in each diffraction image. It is also compatible with using multiple Bragg vector spacings, where the flow line spacing can be adjusted to accurately visualize the relative lattice spacings. Note that in the data sets analysed in this study, the π–π diffraction spacing was dominant, representing the vast majority of diffracted disk intensity.

Data availability

The data that support the findings of this study are available from the corresponding author upon reasonable request.

References

39. Pekin, T. C., Gammer, C., Ciston, J., Minor, A. M. & Ophus, C. Optimizing disk registration algorithms for nanobeam electron diffraction strain mapping. *Ultramicroscopy* **176**, 170–176 (2017).